

# Subsurface Structures at the Chang'e-3 Landing Site: Interpretations from Orbital and In-Situ Imagery Data

Le Qiao, Zhiyong Xiao, Jiannan Zhao, Long Xiao\*

Planetary Science Institute, School of Earth Sciences, China University of Geosciences, Wuhan 430074, China

**ABSTRACT:** The Chang'e-3 (CE-3) spacecraft successfully landed on one of the youngest mare surfaces on the Moon in December 2013. The Yutu rover carried by CE-3 was equipped with a radar system that could reveal subsurface structures in unprecedented details, which would facilitate for understanding regional and global evolutionary history of the Moon. Based on regional geology, cratering scaling, and morphological study, here we quantify the subsurface structures of the landing site using high-resolution orbital and in-situ imagery data. Three layers of lunar regolith, two layers of basalt units, and one layer of ejecta deposits are recognized at the subsurface of the landing site, and their thicknesses are deduced based on the imagery data. These results could serve as essential references for the on-going interpretation of the CE-3 radar data. The ability to validate our theoretical subsurface structure using CE-3 in-situ radar observations will improve the methods for quantifying lunar subsurface structure using crater morphologies and scaling.

**KEY WORDS:** Chang'e-3, subsurface structure, impact cratering, Lunar Penetrating Radar, lunar exploration.

## 0 INTRODUCTION

Subsurface structure of the Moon is a direct record of its long and complex geological evolutionary history. Multi-episodes of magmatic activities produced vast volume of basalts with various chemical compositions both on the lunar surface and within the crust. Long-term space weathering and impact gardening produced a global layer of loose regolith. While meteoritic impact processes, including both primary and secondary impacts, and tectonic activities would additionally complicate the subsurface geology of the Moon. Moreover, these geological activities were usually intertwined with and influenced by each other, which made the subsurface structure further complex. Quantifying the subsurface stratigraphic and tectonic features of the Moon, including basaltic rocks, lunar regolith, and impact breccia deposits, with a depth from a few to hundreds of meters can provide key information for solving scientific mysteries concerning regional and global origin and evolutionary history.

The most direct and effective technique for determining the subsurface structure of the Moon is in-situ investigation. However, due to the high technical demand and cost for conducting lunar surface experiments, few in-situ measurements of the lunar subsurface structure had been carried in human's lunar exploration history. So far the only in-situ experiment was the Surface Electrical Properties (SEP) experiment carried out during

the Apollo 17 mission in 1972, this equipment was carried to explore a portion of the Taurus-Littrow region. The Apollo 17 SEP experiments indicated that subsurface boulders of dimension in the range of 10–300 m were not present within depths of 1–2 km from the surface (Simmons, 1974). Besides, the analyses and interpretations of these in-situ observation data were usually restricted by certain models, and sometimes it was difficult to find a model which satisfied most of the observed results.

Several indirect techniques have been proposed to quantify the subsurface structures of the Moon. For example, using seismic experiments (Nakamura et al., 1975), morphologies and size-frequency distributions of small fresh craters (Fa et al., 2014; Quaide and Oberbeck, 1968), and radar data (Ono et al., 2009; Shkuratov and Bondarenko, 2001) to estimate regolith thicknesses; using crater size-frequency distributions (Hiesinger et al., 2002), excavation depths of large craters that penetrated (or failed to penetrate) through the mare basalts (Thomson et al., 2009), and gravity data (Talwani et al., 1973) to estimate thicknesses of basalt flows; developing empirical scaling laws to estimate thicknesses of crater ejecta (McGetchin et al., 1973). All these methods are essential complements for quantifying the subsurface structure besides in-situ measurements, and they provide important references for analyzing and interpreting lunar surface experiment observations.

In December 2013, China's Chang'e-3 (CE-3) spacecraft, carrying the Yutu (Jade Rabbit) rover, successfully landed on the northern Mare Imbrium at the lunar nearside (Zhao J N et al., 2014). The landing area is one of the youngest mare basalt units on the Moon (Morota et al., 2011; Bugiolacchi and Guest, 2008), which has never been explored before. The rover carries a set of Lunar Penetrating Radars (LPRs) to detect the subsurface information of the Moon (Xiao, 2014). The LPRs consist

\*Corresponding author: longxiao@cug.edu.cn

© China University of Geosciences and Springer-Verlag Berlin Heidelberg 2016

Manuscript received November 18, 2014.

Manuscript accepted March 25, 2015.

of two types of antennas with different working channels, enabling resolving the subsurface structure of the landing site at different depths and vertical resolutions. The Channel 1 antenna was a monopole mounted on the tail of the rover, operated at a central frequency of 60 MHz (VHF band), with over 400 m penetration depth and ~1 m thickness resolution. The Channel 2 has two dipole bow-tie receiving antennas mounted at the bottom of the rover, operated at a central frequency of 500 MHz (UHF band), with over 12 m penetration depth and ~30 cm thickness resolution (Zhao N et al., 2014). The LPRs were scheduled to collect radar echoes of the lunar shallow subsurface materials along the rover traverse path. Observations from the CE-3 LPRs will provide an unprecedented opportunity to investigate the shallow subsurface structure at the landing site. To assist the interpretation of the CE-3 LPRs data, here we quantify the subsurface structures at the landing site of CE-3 using crater morphologies and scaling on both orbital and in-situ imagery data. The mutual validation between the result of this work and CE-3 LPRs data will improve methods for quantifying lunar subsurface structures using crater morphologies and scaling.

## 1 GEOLOGICAL SETTINGS OF THE CE-3 LANDING SITE

The CE-3 spacecraft landed on a flat mare surface (centered at 44.12°N, 19.51°W, Liu Z Q et al., 2014, Fig. 1) in the northern Mare Imbrium. The CE-3 landing site has higher latitude than any previous soft landing sites (Fig. 1). Remote sensing observations proposed a TiO<sub>2</sub> content of ~7 wt.% for the basalts at the landing site (Zhao J N et al., 2014), which is intermediate compared with the high-titanium basalts (Apollo 11 and 17 basalts) and low-titanium basalts (Apollo 12, 15 and feldspathic basalts). The basalts at the landing site are also

substantially richer in olivine and thorium (Th) element compared with the other lunar basalts (Wu et al., 2014; Lucey, 2004; Lawrence et al., 2000). The basalts at the landing site have a higher content of titanium than those ~15 km to the north (TiO<sub>2</sub> ~1.4 wt.%, Zhao J N et al., 2014), indicating two episodes of lava infilling events with different lava compositions. Crater counting results suggested an Imbrian model age (>3.0 Ga) for the basalts to the north, and an Eratosthenian model age (~2.5 Ga) for the basalts of the CE-3 site (Qiao et al., 2014; Morota et al., 2011; Chen et al., 2010; Bugiolacchi and Guest, 2008; Hiesinger et al., 2000), which was much younger than the returned lunar basalt samples (most Apollo basalt samples are dated older than 3.0 Ga, Stöffler and Ryder, 2001). So regional magmatic activities at the CE-3 site generally evolved from Imbrian-aged low-titanium to Eratosthenian-aged medium-titanium. Featuring one of the youngest basalts on the Moon that has not been sampled by any previous missions (Giguere et al., 2000; Papike et al., 1976), the CE-3 landing site is indicative for revealing the nature of late-stage volcanism on the Moon.

## 2 METHODOLOGY

Two units of mare basalts that have different ages have been identified at the CE-3 landing site. Due to the ~0.5 b.y.r age difference between the basalts (Morota et al., 2011; Bugiolacchi and Guest, 2008), a regolith layer must have been formed on the top of the underlying Imbrian basalts. After the formation of the Eratosthenian basalts at ~2.5 Ga, meteorite impacts and space weathering became the major surface processes which have formed a regolith layer on the top of the surface Eratosthenian basalts. Some large crater with diameters of hundreds of meters surrounding the CE-3 landing site might have penetrated (or failed to penetrate) through this regolith

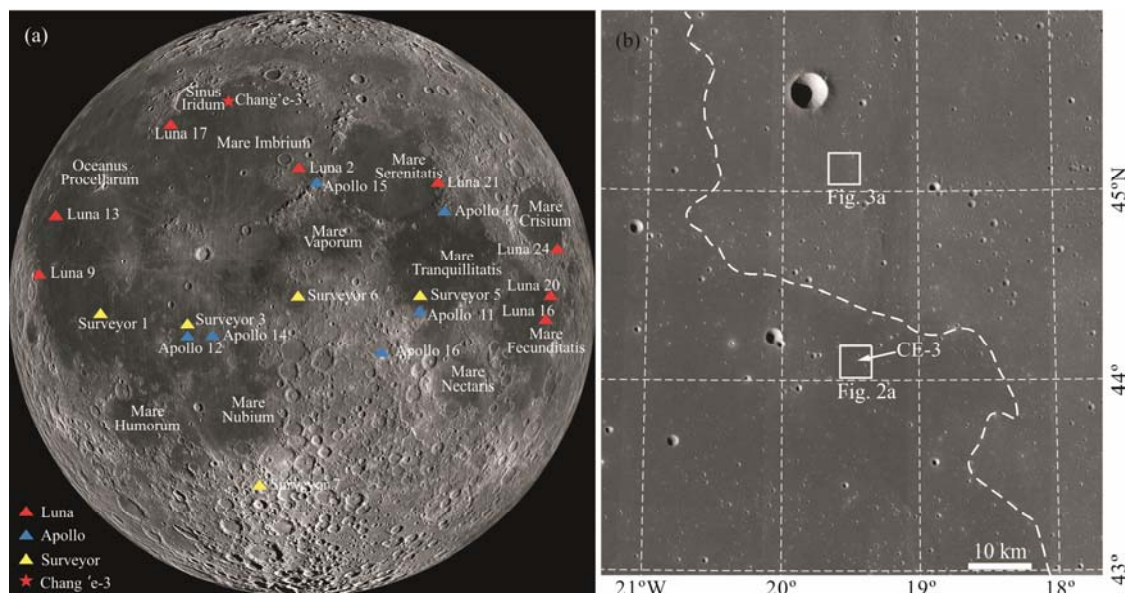


**Figure 1.** (a) Landing sites of the Chang'e-3 and previous soft landing exploration missions. The base map is a mosaic of lunar nearside generated from images acquired by the Lunar Reconnaissance Orbiter (LRO) wide-angle camera (WAC). Image credit: NASA/GSFC/Arizona State University. (b) Local detailed image (LRO WAC mosaic image) of the Chang'e-3 landing site and surrounding areas. The dashed line represents the boundary of medium-titanium basalt unit at landing site and northern low-titanium unit. The arrow points to the landing site. The two rectangles mark the areas where crater counting was performed for determining regolith thickness (Section 3.1). Panel b is Lambert conformal projected and centered at 44.47°N, 19.49°W, and up is the north.

layer reaching the Eratosthenian basalts, and possibly excavated (or failed to excavate) underlying Imbrian low-titanium basalt to surface. The excavation depths of these craters can provide both upper and lower limits for the thickness of the Eratosthenian basalts (Thomson et al., 2009). Small fresh craters with diameters of tens of meters mainly form within the surface regolith layer. The morphologies of these small crater may not be identical, e.g., normal, concentric or flat-bottom, depending on the ratio of the crater diameter to the regolith thickness. We can thus estimate the regolith thickness based on observations of small fresh craters' morphologies and diameters (Fa et al., 2014; Quaide and Oberbeck, 1968; Oberbeck and Quaide, 1967). The CE-3 spacecraft landed on the continuous ejecta blanket of a large crater (i.e., Chang'e crater; Zhao J N et al., 2014), so the ejecta deposits are also essential parts of subsurface geological features (McGetchin et al., 1973). Therefore, the layered subsurface structures at the CE-3 landing site could be schematically revealed from the photogeology interpretation and geological background study, with three layers of lunar regolith, one layer of crater ejecta materials, and two layers of basalts. Here we focus on the thicknesses of each layer.

### 2.1 Dating Determining Lunar Regolith Thickness

Referring to the usage of morphology and size of small fresh craters can provide the highest accuracy to estimate the thickness of surface regolith (Fa et al., 2014; Quaide and Oberbeck, 1968), especially after the release of high-resolution imaging data obtained by LRO narrow-angle camera (NAC). The NAC was onboard NASA LRO spacecraft launched in 2009, and can image the lunar surface at a monochrome band with a resolution of 0.5–2 m/pixel. Here we use this method and LRO NAC images to determine the lunar regolith thicknesses at the CE-3 landing site.

Small fresh craters with normal, flat-bottomed and concentric geomorphologies are widespread on the lunar surface. Laboratory experiments suggested that craters with different geomorphologies could be formed when meteoroids impact a layer of unconsolidated materials (e.g., lunar regolith) with underlying more cohesive substrates (e.g., bedrock; Oberbeck and Quaide, 1967). The morphologies of small crater are related to the ratio ( $R$ ) of the rim-to-rim diameter of a crater ( $D$ ) to the regolith thickness ( $T$ ). When  $R$  is less than 3.8–4.2, complete crater growth occurred and thus a bowl-shaped normal crater forms. A concentric crater would form when  $R$  is greater than 8–10 (Fa et al., 2014; Quaide and Oberbeck, 1968; Oberbeck and Quaide, 1967). When  $R$  is between the value that forms a concentric and a normal crater, the cohesive substrates interfere with crater growth, forming a flat-bottomed crater. By counting the size-frequency distributions of small fresh craters with variable geomorphologies within a local geological setting, we can make an estimation for the regional regolith thickness. Using LRO NAC images, we studied the morphologies and measured the size-frequency distributions of small fresh craters to determine the lunar regolith thickness on the top of the surface Eratosthenian basalts. Also, we counted small craters at the northern Imbrian basalts to deduce the regolith thickness on the top of the underlying Imbrian basalts.

### 2.2 Estimating Ejecta Deposits Thickness

Determining the radial thickness of lunar impact crater ejecta deposits has been fraught with controversies. In works published between 1791 and 1802, the Germany astronomer Schröter developed his "rule" by suggesting that the volume of the crater rim deposits usually equaled that of the crater bowl (e.g., Pike, 1967). While modern studies indicated that Schröter's observation could be only verified for explosion-produced craters where the original ground surface was clearly marked (e.g., Melosh, 1989). Laboratory hypervelocity impact experiments (e.g., Stöffler et al., 1975) and investigations of explosion-produced craters (Cooper, 1977; Carlson and Jones, 1965) indicated that large amount of uplifted substrate materials should be incorporated in crater rim, and ejecta comprised 60%–80% of the total rim height. Based on the widely cited compilation of data from explosion-produced craters, laboratory synthetic craters, and natural meteoroid impact craters, McGetchin et al. (1973) proposed an empirical calculation for predicating radial thickness variation of lunar crater ejecta

$$t=0.14 \cdot R^{0.74} \cdot (r/R)^{-3.0} \quad (1)$$

where  $t$  is the ejecta thickness,  $R$  is the crater radius, and  $r$  is the distance from the crater center. By reliable measurements of the diameter of the Chang'e crater and distance from the CE-3 site to the crater center, we can thus estimate the ejecta deposits thickness at CE-3 landing site. In this work, the crater dimension was recognized and measured on the SELENE Terrain Camera (TC) DTM topography data. The TC DTM topography data was derived from TC stereo pair images by the imaging team, which has a spatial sampling resolution of ~10 m/pixel, the highest-resolution global topography data set for now (Haruyama et al., 2012). While the distance of the investigated site from the crater center was measured on the LRO NAC image.

### 2.3 Quantifying Mare Basalts Thickness

Among the various techniques for determining the thickness of individual and/or accumulated lava flow, the utilization of crater excavation depths provide the best accuracy (Qiao et al., 2014; Thomson et al., 2009). Thomson et al. (2009) used this method to estimate the accumulated thickness of basalt flows in the Mare Imbrium region, and constrained the accumulated basalt thickness at the CE-3 landing site as ~1 km.

This technique was also appropriate for individual lava flow unit in regions where the basaltic layers at the surface and the depths showed distinctly compositional differences (Qiao et al., 2014). In such cases, some larger craters spread on the surficial basalt deposits might penetrate through the uppermost basaltic layer and excavate underlying materials with different compositions, thus produced a compositionally inhomogeneous crater rim. The excavation depths of these relatively larger craters can constrain the upper limit of thickness of uppermost basalt unit. While some other smaller craters might fail to penetrate through the surface basalt unit, and thus exhibit a homogenous crater rim. The excavation depths of these relatively smaller craters can provide lower constraints for the thickness of individual basalt unit.

Using SELENE Multiband Imager (MI) data and algorithm proposed by Otake et al. (2014), we calculate titanium

content for both the ejecta materials and background terrain of craters surrounding the CE-3 site to distinguish whether or not a crater had penetrated the surface Eratosthenian basalt unit. The SELENE MI can image the lunar surface with a spatial resolution of 20 m in five visible bands and 62 m in four near-infrared bands from the 100 km orbit altitude. The crater excavation depth can be reckoned from crater diameter, because the excavation depth scales with crater diameter (0.084 for simple crater; Melosh, 1989). By investigating the size and titanium content of craters spread on the Eratosthenian basalt deposits surrounding the CE-3 site, we can constrain the thickness of Eratosthenian basalt unit.

### 3 RESULTS

#### 3.1 Thicknesses of Lunar Regolith Layers

##### 3.1.1 Regolith thickness on the top of the Eratosthenian and Imbrian basalts

We chose two 5×5 km square areas (Fig. 1b) at the landing site and northern Imbrian basalts to perform the morphology recognition and size-frequency distribution measurements of small fresh craters. The two working areas were away from geologic unit boundaries, tectonic landforms, and large craters to eliminate disturbances on the regolith thickness estimation. The LRO NAC frame M1129602407L was used to count craters (1.56 m/pixel), because this NAC frame has relatively large incidence angle (58.88°) to support reliable morphologic interpretations of lunar small fresh craters. The solar elevation angle of NAC frame M1129602407L (complementary angle of incidence angle) is larger than the repose angle of lunar regolith (taken as 31°, Quaide and Oberbeck, 1968), which eliminates the errors in recognizing crater with various morphologies produced by very low solar elevation angles (Fa et al., 2014). This NAC image was map-projected in a Lambert conformal projection and centered at the landing site, because this projection caused little distortion in mid-latitudes areas (Snyder, 1987). Craters with diameters between 10 and 250 m in the NAC image were counted and classified morphologically. Only fresh craters were counted and classified based on their geomorphological features, e.g., rays, halos, sharp rims (Oberbeck and Quaide, 1967). The characteristic shadow pattern of each crater on optical imaging data was used to distinguish their morphological types. Normal craters usually have conical or spherical segment shadow shapes as deduced from their completely arcuate shadow patterns. The flat-bottomed craters, with pronounced flat floors, present single annular shadow patterns, and some develop a well-defined central mound. While concentric craters, featured by a nested crater structure, exhibit double annular or annular arcuate shadow patterns (Oberbeck and Quaide, 1967).

The distribution of all the observed small normal, flat-bottomed and concentric craters surrounding the landing site in the 5×5 km square area is shown in Fig. 2a. We also plotted the diameter-frequency distribution for these craters (Fig. 2b). To reveal the relative proportion of each morphological type crater occurring at each diameter interval, the absolute crater count data had been re-plotted in Fig. 2c. Over 90% of fresh craters with diameters less than 21 m were normal craters, and fresh craters with diameters between 37 to 53 m

were dominantly flat-bottomed. Over 90% of fresh crater with diameters larger than 57 m were concentric. Since the normal craters can constrain the lower limit of the regolith thickness (between  $D/4.2$  to  $D/3.8$ ), and concentric craters constrain the upper limit (between  $D/10$  to  $D/8$ , Quaide and Oberbeck, 1968), the average regolith thickness on the top of the Eratosthenian basalt deposits surrounding the CE-3 landing site was estimated as 5 to 6 m, which is consistent with the result (5–7 m) of Liu T T et al. (2014), and Shkuratov and Bondarenko (~6 m, 2001).

We also investigated the size-frequency distributions and geomorphologies of small fresh craters in the northern Imbrian low-titanium basalt deposits (Fig. 3a). The absolute number and percentage of each type craters at each diameter interval were plotted in Figs. 3b and 3c, respectively. Crater counting results revealed that over 90% of small fresh craters with diameter less than 25 m were normal crater, and craters with diameter between 33 and 49 m were dominantly flat-bottomed. Over 90% of fresh craters with diameters larger than 61 m were concentric. The average regolith thickness at the northern Imbrian basalts was thus estimated as 6–7 m. As the regolith layer accumulated on the underlying Imbrian basalts formed during the time gap between the two major lava flow infilling events (~0.5 Ga, Qiao et al., 2014; Bugiolacchi and Guest, 2008; Hiesinger et al., 2002), the thickness of the regolith on the top of the Imbrian basalts can be calculated as the difference between the regolith thickness at the surface basalt unit surrounding CE-3 landing site and at the northern areas, i.e., about 1 m.

##### 3.1.2 Regolith thickness at the continuous ejecta blanket of Chang'e crater

Very few small fresh craters with flat-bottomed and/or concentric morphologies are visible on the continuous ejecta blanket of the Chang'e crater. Thus, we could not get reliable constraints on the regolith thickness at the continuous ejecta blanket using morphologies and sizes of small fresh craters. We alternatively refer to excavation depths of small craters (several to tens of meters in diameter) using images taken by the CE-3 landing camera (LCAM) to make an approximate estimation for the surficial regolith thickness at the ejecta blanket. The usage of crater excavation depths had been widely adopted for determining mare basalt thickness (e.g., Section 3.3; Qiao et al., 2014; Thomson et al., 2009).

The CE-3 LCAM was mounted on the CE-3 lander for taking images of the landing area during the soft landing process, the best resolution is about centimeters per pixel. We here chose the CE-3 LCAM frame 3006 (Fig. 4) to investigate the regolith thickness on the ejecta blanket. This image was taken on December 14, 2013 (UTC) with a spatial resolution of about 0.1 m/pixel and at a solar elevation of ~24° (Lu et al., 2014). Many small craters with diameters of several centimeters to tens of meters are visible on the continuous ejecta blanket. These craters have different diameters, excavation depths, and crater wall morphologies. Some relatively large craters had penetrated through the uppermost regolith layer and excavated subsurface boulders of the ejecta blanket, and thus developed a pronounced rocky inner wall with massive boulders. While some small craters failed to penetrate the uppermost regolith layer, and had a homogeneous inner wall covered by loose



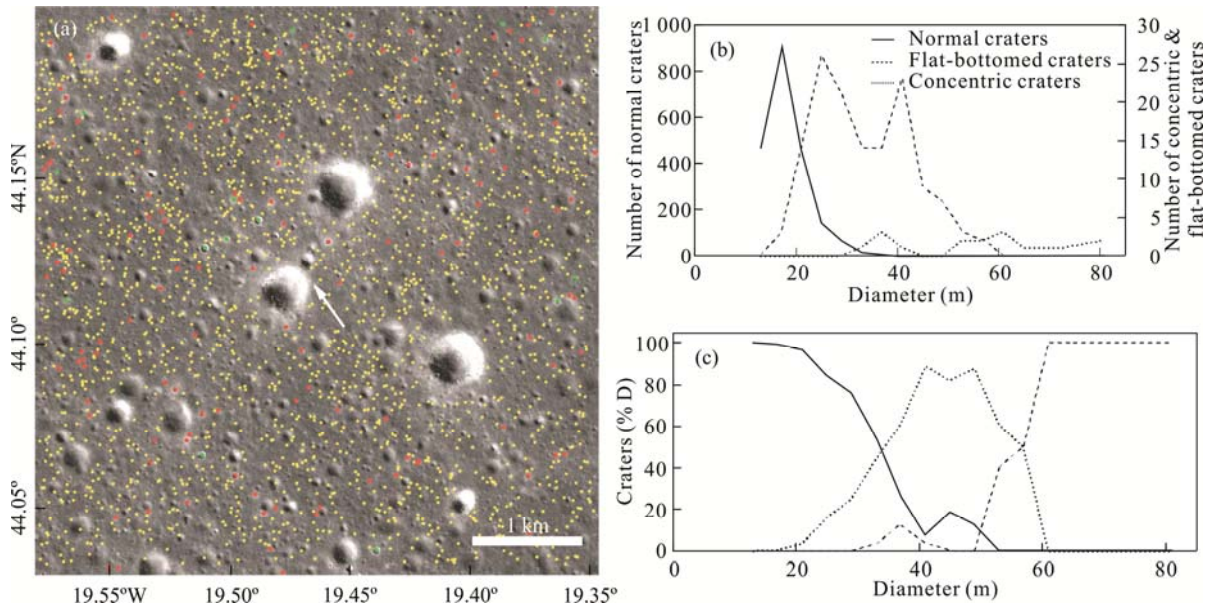


**Figure 2.** (a) Spatial distribution of all observed small normal, concentric and flat-bottomed craters surrounding the CE-3 landing site, with yellow ones for normal craters, red ones for flat-bottomed craters and green ones for concentric craters. The landing site is pointed by the white arrow. The base map is LRO NAC frame M1129602407L projected in Lambert conformal projection and centered at the landing site, and up is the north. (b) Absolute counts for observed craters. (c) Percentage of normal, concentric and flat-bottomed craters at each diameter interval  $D$ .

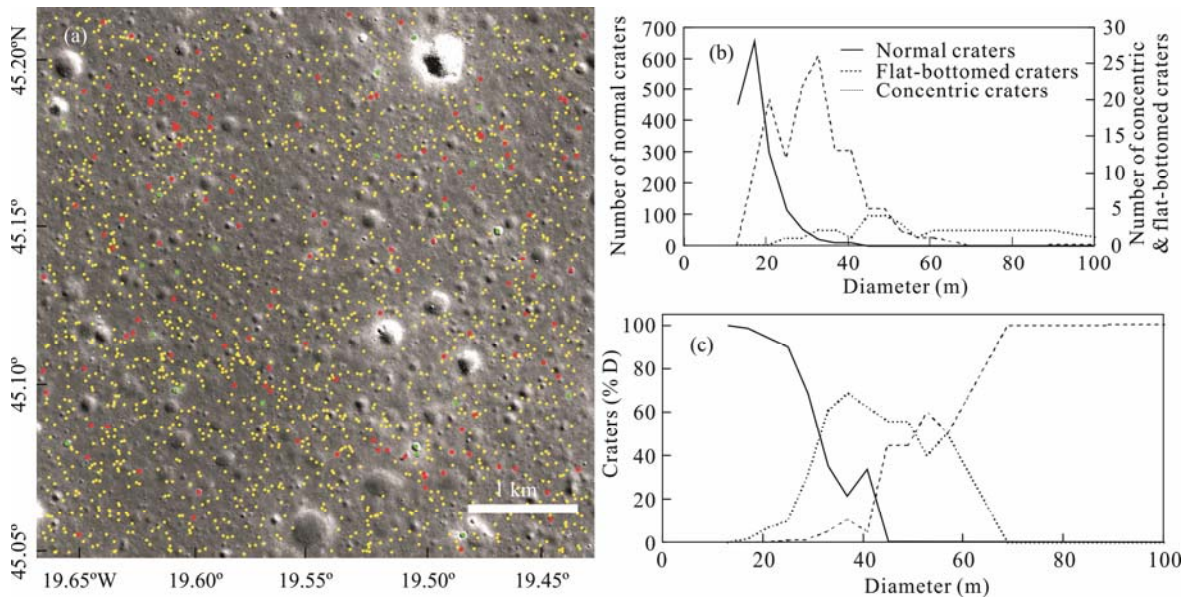


**Figure 3.** (a) The distribution of counted small crater with various morphological features in the 5×5 km square area at the northern Imbrium basalt deposits, with yellow ones for normal craters, red ones for flat-bottomed craters and green ones for concentric craters. The based map is a segment of LRO NAC frame M1129602407L projected in Lambert conformal projection and centered at 45.13°N, 19.51°W, and up is the north. (b) Absolute counts for the observed craters. (c) Percentage of normal, concentric and flat-bottomed craters at each diameter interval  $D$ .

regolith materials. We investigated all regional larger craters surrounding the CE-3 landing site (Fig. 4), measured their rim-to-rim diameters and characterized the morphological features of the inner crater walls. Seven craters with diameters larger than 4 m occurred on the continuous ejecta blanket, and the inner wall of the 13-meter-diameter and 17-meter-diameter craters exposed massive boulders excavated from the underlying ejecta blanket, while other small craters, with diameter less than 11 m, might have not penetrated the surface regolith layer exhibiting regolith-mantling inner walls. Therefore, the surface

regolith thickness at the continuous ejecta blanket was estimated to be ~1 m judging from the morphologies and excavation depths (reckoned from diameter) of these small craters.

### 3.2 Ejecta Deposit Thickness

When using the McGetchin’s algorithm (Eq. 1) to determine the ejecta thickness at the CE-3 landing site, it is crucial to make an accurate measurement for the radius of Chang’e crater and distance from the landing site to the crater center, especially for the degraded Chang’e crater with reduced

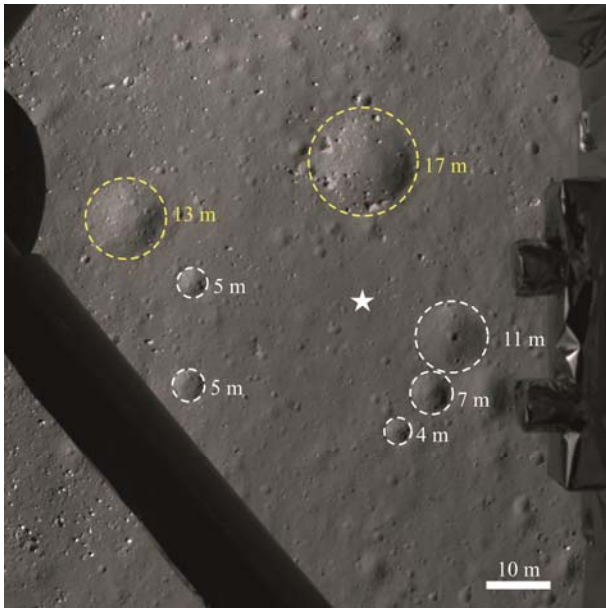


**Figure 4.** Image of the CE-3 landing area taken by CE-3 LCAM. All craters investigated for determining the regolith thickness are marked by white dashed circles, with their diameters labeled. The yellow circles are craters believed to have penetrated the surface regolith layer, and the white ones are craters failed to penetrate the surface regolith. The white star denotes the CE-3 landing site. Image ID is CE3\_BMYK\_LCAM-3006, and up is the north.

sharpness of the rim. To measure the diameter of this crater, we extracted 9 radial topography profiles across the crater center from the SELENE TC DTM topography data ( $\sim 10$  m/pixel, Haruyama et al., 2012) with  $20^\circ$  increments. In each profile, points where the elevation reached regional maximum was regarded as the rim crest, and the distance between two rim crests was defined as the crater diameter (Fig. 5a). Three elevation profiles were neglected because the distractions of subsequent new craters, which effaced the original rim crest features. The measured diameters were averaged as the diameter of the Chang'e crater, i.e.,  $\sim 475$  m. The distance of CE-3 landing site from the rim crest was measured as  $\sim 45$  m (Fig. 5b) on LRO

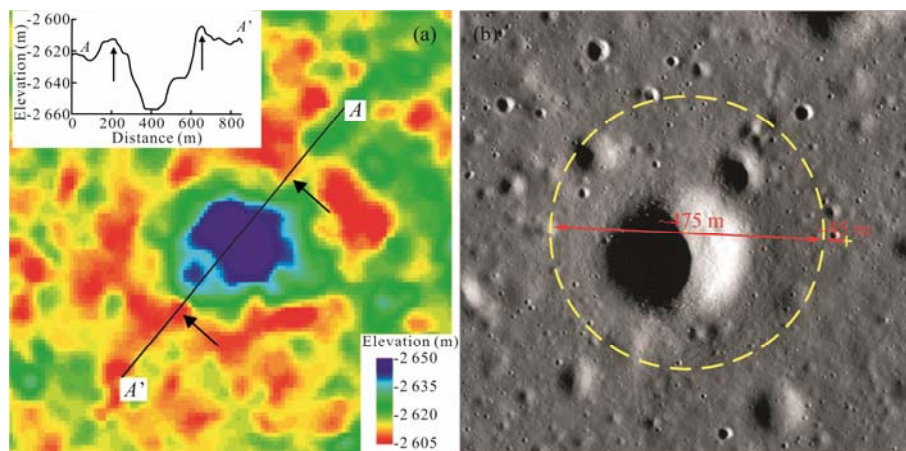


**Figure 5.** (a) SELENE TC DTM topography data of the CE-3 landing area. A sample of radial elevation profiles (A–A') shows regional maximum values (denoted by black arrows) inferred as the rim crest position. (b) The LRO NAC frame M102285549L of the landing area, the approximate location of the crater rim crest and the landing site was marked by the yellow circle and the cross, respectively. All panels are in Lambert conformal projection and centered at the landing site, up is the north.

NAC frame M102285549L (pixel size  $\sim 1.66$  m and incidence angle  $80.85^\circ$ ). Using the algorithm proposed by McGetchin (Eq. 1), the ejecta deposit thickness at the CE-3 landing site was estimated as  $\sim 5$  m.

### 3.3 Thickness of the Eratosthenian Basalt

The distinctly compositional difference between the surface Eratosthenian and underlying Imbrian basalts provided an excellent setting for estimating the Eratosthenian basalt unit thickness using crater excavation depths (Section 2.3). We mapped the titanium content surrounding the CE-3 landing site using SELENE MI data and algorithm proposed by Otake et al. (2014; Fig. 6). The SELENE MI data has been calibrated, geometric registered, and mosaicked into  $1^\circ \times 1^\circ$  block by the imaging team (<http://l2db.selene.darts.isas.jaxa.jp>). The areas outside the two vertical seam lines on the titanium map (Fig. 6) caused by mosaicking multi images were avoided when calculating the Eratosthenian basalt thickness.

We investigated all craters  $>400$  m in diameter surrounding the CE-3 landing site and measured their rim-to-rim diameters (Table 1, Fig. 6). Some craters near to the Eratosthenian and Imbrian basalt boundary, where the thickness of Eratosthenian basalt unit was predicted to be much thinner, were neglected during measurements. We also determined whether a crater had penetrated the uppermost Eratosthenian medium-titanium basalt unit according to the titanium content of ejecta materials, and calculated its excavation depth. The thickness of the Eratosthenian basalt unit was thus constrained between 45 and 48 m. Using shadow measurements on imaging data obtained with low-sun angles, Schaber (1973) reported an average thickness of 30–35 m (range 10–63 m) for the Eratosthenian flows in Mare Imbrium. Hiesinger et al. (2002) suggested a thickness of 32–50 m ( $+11/-5$  m) for this basalt flow unit based on the shape of crater size-frequency distribution curves. Our results are well consistent with previous results, while can provide the highest accuracy. Compared with  $\sim 1$  km thickness of the underlying and older Imbrian basalt deposits (Thomson et al., 2009), the Eratosthenian volcanism at the Mare Imbrium region characterized a sharp decrease of volcanic flux.



**Table 1** The investigated craters surrounding CE-3 landing site for determining Eratosthenian mare (Em) basalt unit thickness. The No. 1 crater is the Chang'e crater, whose ejecta blanket CE-3 landed on. The craters numbers correspond to those in Fig. 6.

No.	Lat (°N)	Lon (°W)	Diameter (m)	Excavation depth (m)	Basalt thickness (m)	Penetration of Em basalt (Y/N)
1	44.12	19.52	470	39	>39	N
2	44.15	19.50	530	45	>45	N
3	44.10	19.45	490	41	>41	N
4	44.20	19.34	740	62	<62	Y
5	44.25	19.26	640	54	<54	Y
6	44.26	19.21	700	59	<59	Y
7	44.00	19.29	780	66	<66	Y
8	43.92	19.41	490	41	>41	N
9	43.86	19.38	620	52	<52	Y
10	43.95	19.54	470	39	>39	N
11	43.95	19.59	570	48	<48	Y
12	44.05	19.75	510	43	>43	N
13	44.19	19.65	530	45	>45	N
14	44.22	19.64	460	39	>39	N

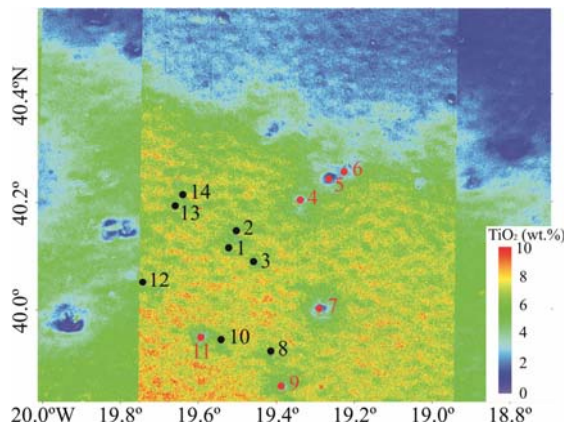


**Figure 6.** TiO<sub>2</sub> content map of mare basalts surrounding the CE-3 landing site, calculated from SELENE MI data and [Otake et al.'s algorithm \(2014\)](#). The crater measurements were performed within the uniform imaging area between the two seam lines to eliminate the distractions of mosaicking multi-images that have different imaging conditions. All craters measured for determining Eratosthenian basalt unit thickness are marked by dots, with their numbers labeled (correspond to those in Table 1). The red dots are craters which have penetrated the Eratosthenian basaltic layer, and the black ones are craters which failed to penetrate the Eratosthenian basalt. The No. 1 crater is the Chang'e crater, whose ejecta blanket CE-3 landed on. The map is in Lambert conformal projection centered at 44.5°N, 19.5°W.

## 4 DISCUSSION AND CONCLUSION

### 4.1 Simplifications and Limitations

Several simplifications have been made for the interpreted layered subsurface structures at the CE-3 landing site in this work. First, regional tectonic activities, which would further complicate the subsurface structures, was not considered when quantifying regional subsurface structures. At least five sets of wrinkle ridges, generally believed to be purely tectonic landforms (e.g., Golombek et al., 1991), were recognized near the CE-3 landing site (Zhao J N et al., 2014). And some of these wrinkle ridges directly cut across the Chang'e crater. Second, the continuous meteoritic impacts would fragment the original bed rock and produce a global layer of chaotically mixed impact debris, termed “mega-

regolith” (Hiesinger and Head, 2006), of which most part were not considered in this work except the fine-grained surface regolith (Section 3.1). Then, given the rather small thickness of regolith layer on the top of the Imbrian basalt (estimated as ~1 m thick in Section 3.1.1), we should be aware of the possibility of assimilation of this regolith layer by the subsequent and overlying Eratosthenian basalts (estimated as 45–48 m thick in Section 3.3), which may obstruct the detection of this thin regolith layer by the CE-3/Yutu LPRs. Besides, while we have tried to minimize the possible effects of the MI spectral imaging data on the calculation of TiO<sub>2</sub> content for determining the Eratosthenian basalt thickness, we should be cautious of the ubiquitous errors of quantifying surface element content from orbiter spectral data caused by a series of factors, e.g., topography and illumination conditions.

Lastly, although two sets of basalt units, corresponding to two major lava infilling events, were identified in this work, the actual eruptional history was more complex. A major episode of lava infilling might have not finished in a single continuous period, but in several discrete and near subperiods, thus generated some sublayers of basalt deposits with similar compositions. These simplifications and limitations of this study also caution us the significance and urgency to get new “ground truth” of lunar subsurface geology from in-situ experiments.

### 4.2 Subsurface Structures at the Chang'e-3 Landing Site

Based on the regional geological settings at the CE-3 landing site (Section 1) and estimated thicknesses of the three regolith layers, ejecta deposits, and Eratosthenian mare basalt unit, a schematic multi-layered subsurface structure model of the CE-3 landing site was illustrated (Fig. 7). Compared with previous Apollo and Luna landing sites (e.g., Spudis and Pieters, 1991), the subsurface structures at CE-3 landing site show unique geological characteristics in multi-layers of regolith, two sets of mare basalts with distinct titanium content difference. Although some of previous lunar landing sites, i.e., Apollo 11, 12 and 15 also characterize subsurface structures of multiple chemically distinct groups of mare basalts, those basalts of different groups at one

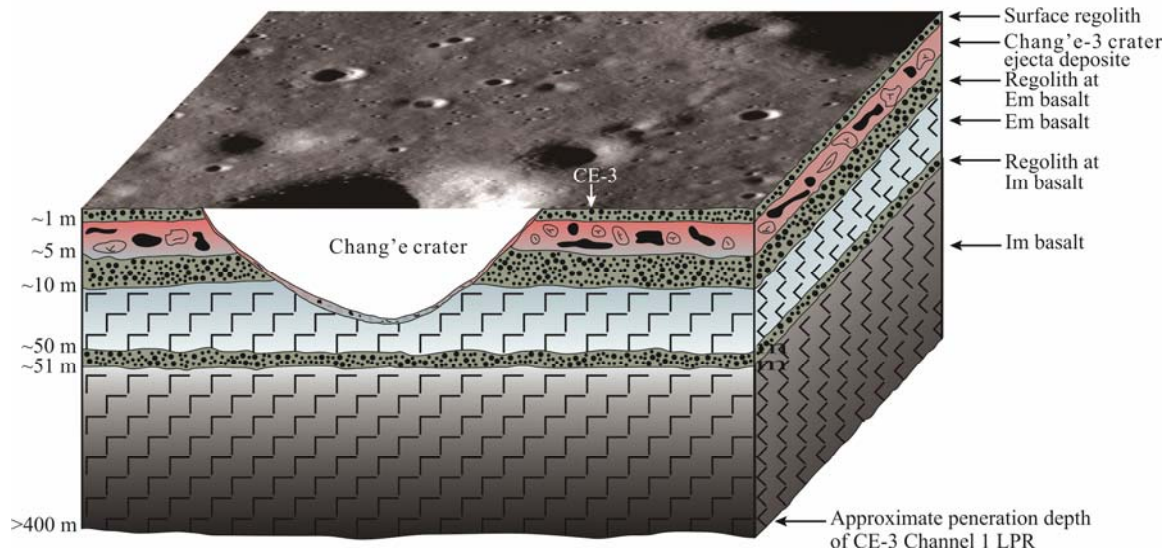


**Figure 7.** East-to-west schematic geological cross-section through the shallow subsurface of the CE-3 landing site. The CE-3 landing site and Chang'e crater are denoted. The surface image is from LRO NAC frame M102285549L. The schematic model is not mapped in geometry scale both in vertical and horizontal, for better illustrating the multiple subsurface layers with thicknesses at different magnitudes.

site show similar titanium content. While the two groups of mare basalts at the subsurface of CE-3 landing site, i.e., the Eratosthenian and Imbrian basalts, show apparently different titanium content, thus can be classified into different basalt types. The Imbrian basalts can be grouped into typical low-titanium basalt, while the Eratosthenian basalts can be classified as medium-titanium basalt (Giguere et al., 2000). The thickness estimation of the Eratosthenian basalts, both by optical imaging data and surface in-situ radar measurements, will provide basic constraints for volcanic flux estimates of lunar late-stage volcanism. The three regolith layers at various depths with different thicknesses and production times, provide an ideal target for validating the method of using morphologies and sizes of small fresh craters for determining lunar regolith thickness.

#### 4.3 Implications for CE-3 LPRs Data Interpretation

In-situ radar experiments by LPRs onboard CE-3/Yutu rover provide an unprecedented opportunity to study the shallow subsurface geology at the northern Mare Imbrium. While processing and interpretation of GPRs data usually depend on certain geophysical models and should consider regional geological settings. The theoretical, while quantitative layered subsurface structures and regional geological setting derived from imaging data in this study can provide essential references for CE-3 LPRs data processing and application. Additionally, the CE-3 LPRs observation results can also be used to validate and improve the methods for determining thickness of regolith, mare basalt and ejecta deposits employed in this work.

#### ACKNOWLEDGMENTS

The authors are grateful to the editors and the two anonymous reviewers for thoughtful and constructive comments for this paper. We acknowledge the Ground Application System for Chinese Lunar Exploration and Beijing Institute of Space Mechanics and Electricity for providing CE-3 data. We thank Dr. Wenzhe Fa and Ms. Tiantian Liu at Peking Univer-

sity for instructions on calculating regolith thickness. This work was supported by the Key Research Program of the Chinese Academy of Sciences (No. KGZD-EW-603), the National Natural Science Foundation of China (Nos. 41373066, 41403053), and the State Scholarship Fund of China (No. 201406410040). The final publication is available at Springer via <http://dx.doi.org/10.1007/s12583-015-0655-3>.

#### REFERENCES CITED

- Bugiolacchi, R., Guest, J., 2008. Compositional and Temporal Investigation of Exposed Lunar Basalts in the Mare Imbrium Region. *Icarus*, 197(1): 1–18. doi:10.1016/j.icarus.2008.04.001
- Carlson, R. H., Jones, G. D., 1965. Distribution of Ejecta from Cratering Explosions in Soils. *Journal of Geophysical Research*, 70(8): 1897–1910. doi:10.1029/jz070i008p01897
- Chen, S. B., Meng, Z. G., Cui, T. F., et al., 2010. Geologic Investigation and Mapping of the Sinus Iridum Quadrangle from Clementine, SELENE, and Chang'e-1 Data. *Science China Physics, Mechanics and Astronomy*, 53(12): 2179–2187. doi:10.1007/s11433-010-4160-5
- Cooper, H. F., 1977. A Summary of Explosion Cratering Phenomena Relevant to Meteor Impact Events. In: Roddy, D. J., Pepin, R. O., Merrill, R. B., eds., *Impact and Explosion Cratering: Planetary and Terrestrial Implications*. Pergamon Press, New York. 11–44
- Fa, W. Z., Liu, T. T., Zhu, M. H., et al., 2014. Regolith Thickness over Sinus Iridum: Results from Morphology and Size-Frequency Distribution of Small Impact Craters. *Journal of Geophysical Research: Planets*, 119(8): 1914–1935. doi:10.1002/2013je004604
- Giguere, T. A., Taylor, G. J., Hawke, B. R., et al., 2000. The Titanium Contents of Lunar Mare Basalts. *Meteoritics & Planetary Science*, 35(1): 193–200. doi:10.1111/j.1945-5100.2000.tb01985.x
- Golombek, M. P., Plescia, J. B., Franklin, B. J., 1991. Faulting and Folding in the Formation of Planetary Wrinkle Ridges. In:



- Proceedings of the Lunar and Planetary Science Volume 21, Houston, USA. 679–693
- Haruyama, J., Hara, S., Hioki, K., et al., 2012. Lunar Global Digital Terrain Model Dataset Produced from SELENE (Kaguya) Terrain Camera Stereo Observations. In: Proceedings of 43rd Lunar and Planetary Institute Science Conference, Woodlands, USA. Abstract 1200
- Hiesinger, H., Head, J. W., 2006. New Views of Lunar Geosciences: An Introduction and Overview. In: Jolliff, B. L., Wieczorek, M. A., Shearer, C. K., et al., eds., *New View of the Moon*. Mineralogy Society of American, Chantilly. 28–29
- Hiesinger, H., Jaumann, R., Neukum, G., et al., 2000. Ages of Mare Basalts on the Lunar Nearside. *Journal of Geophysical Research: Planets*, 105(E12): 29239–29275. doi:10.1029/2000je001244
- Hiesinger, H., Head, J. W., Wolf, U., et al., 2002. Lunar Mare Basalt Flow Units: Thicknesses Determined from Crater Size-Frequency Distributions. *Geophysical Research Letters*, 29(8): 89-1–89-4. doi:10.1029/2002gl014847
- Lawrence, D. J., Feldman, W. C., Barraclough, B. L., et al., 2000. Thorium Abundances on the Lunar Surface. *Journal of Geophysical Research: Planets*, 105(E8): 20307–20331. doi:10.1029/1999je001177
- Liu, T. T., Fa, W. Z., Zhu, M. H., et al. 2014. Regolith Thickness Estimation over Sinus Iridum Using Morphology and Size-Frequency Distribution of Small Craters from LROC Images. In: Proceedings of 45th Lunar and Planetary Science Conference, Woodlands, USA. Abstract 1347
- Liu, Z. Q., Di, K. C., Peng, M., et al., 2014. High Precision Landing Site Mapping and Rover Localization for Chang'e-3 Mission. *Science China Physics, Mechanics & Astronomy*, 58(1): 1–11. doi:10.1007/s11433-014-5612-0
- Lucey, P. G., 2004. Mineral Maps of the Moon. *Geophysical Research Letters*, 31(8): L08701. doi:10.1029/2003gl019406
- Lu, Y., Basilevsky, A., Abdrakhimov, A., 2014. Local Geology of Chang'e-3 Landing Site from Analysis of the CE-3 Descent Camera and LROC NAC Images. In: Proceedings of 45th Lunar and Planetary Science Conference, Woodlands, USA. Abstract 1116
- McGetchin, T. R., Settle, M., Head, J. W., 1973. Radial Thickness Variation in Impact Crater Ejecta: Implications for Lunar Basin Deposits. *Earth and Planetary Science Letters*, 20(2): 226–236. doi:10.1016/0012-821x(73)90162-3
- Melosh, H. J., 1989. *Impact Cratering: A Geologic Process*. Oxford University Press, New York
- Morota, T., Haruyama, J., Ohtake, M., et al., 2011. Timing and Characteristics of the Latest Mare Eruption on the Moon. *Earth and Planetary Science Letters*, 302(3/4): 255–266. doi:10.1016/j.epsl.2010.12.028
- Nakamura, Y., Dorman, J., Duennebie, F., et al., 1975. Shallow Lunar Structure Determined from the Passive Seismic Experiment. *The Moon*, 13(1–3): 57–66. doi:10.1007/bf00567507
- Oberbeck, V. R., Quaide, W. L., 1967. Estimated Thickness of a Fragmental Surface Layer of Oceanus Procellarum. *Journal of Geophysical Research*, 72(18): 4697–4704. doi:10.1029/jz072i018p04697
- Otake, H., Ohtake, M., Hirata, N., 2014. Lunar Iron and Titanium Abundance Algorithms Based on SELENE (Kaguya) Multi-band Imager Data. In: Proceedings of 43rd Lunar and Planetary Institute Science Conference
- Ono, T., Kumamoto, A., Nakagawa, H., et al., 2009. Lunar Radar Sounder Observations of Subsurface Layers under the Near-side Maria of the Moon. *Science*, 323(5916): 909–912. doi:10.1126/science.1165988
- Papike, J. J., Hodges, F. N., Bence, A. E., et al., 1976. Mare Basalts: Crystal Chemistry, Mineralogy, and Petrology. *Reviews of Geophysics*, 14(4): 475–540. doi:10.1029/rg014i004p00475
- Pike, R. J., 1967. Schroeter's Rule and the Modification of Lunar Crater Impact Morphology. *Journal of Geophysical Research*, 72(8): 2099–2106. doi:10.1029/jz072i008p02099
- Qiao, L., Xiao, L., Zhao, J. N., et al., 2014. Geological Features and Evolution History of Sinus Iridum, the Moon. *Planetary and Space Science*, 101: 37–52. doi:10.1016/j.pss.2014.06.007
- Quaide, W. L., Oberbeck, V. R., 1968. Thickness Determinations of the Lunar Surface Layer from Lunar Impact Craters. *Journal of Geophysical Research*, 73(16): 5247–5270. doi:10.1029/jb073i016p05247
- Schaber, G. G., 1973. Lava Flows in Mare Imbrium: Geologic Evaluation from Apollo Orbital Photography. In: Proceedings of 4th Lunar Science Conference, 73–92
- Shkuratov, Y. G., Bondarenko, N. V., 2001. Regolith Layer Thickness Mapping of the Moon by Radar and Optical Data. *Icarus*, 149(2): 329–338. doi:10.1006/icar.2000.6545
- Simmons, G., 1974. Final Report on the Surface Electrical Properties Experiment. Apollo 17 Preliminary Science Report
- Snyder, J. P., 1987. *Map Projections—A Working Manual*. US Government Printing, Washington, D.C.
- Spudis, P., Pieters, C., 1991. Global and Regional Data about the Moon. In: Heiken, G. H., Vaniman, D. T., French, B. M., et al., eds., *Lunar Sourcebook*. Cambridge University Press, New York. 609–632
- Stöffler, D., Gault, D. E., Wedekind, J., et al., 1975. Experimental Hypervelocity Impact into Quartz Sand: Distribution and Shock Metamorphism of Ejecta. *Journal of Geophysical Research*, 80(29): 4062–4077. doi:10.1029/jb080i029p04062
- Talwani, M., Thompson, G., Dent, B., et al. 1973. Traverse Gravimeter Experiment. Apollo 17 Preliminary Science Report
- Thomson, B. J., Grosfils, E. B., Bussey, D. B. J., et al., 2009. A New Technique for Estimating the Thickness of Mare Basalts in Imbrium Basin. *Geophysical Research Letters*, 36(12): L12201. doi:10.1029/2009gl0137600
- Wu, Y. Z., Head, J. W., Pieters, C. M., et al. 2014. Regional Geology of the Chang'e-3 Landing Zone. In: Proceedings of 45th Lunar and Planetary Science Conference, Woodlands, USA. Abstract 2613
- Xiao, L., 2014. China's Touch on the Moon. *Nature Geoscience*, 7(6): 391–392. doi:10.1038/ngeo2175
- Zhao, J. N., Huang, J., Qiao, L., et al., 2014. Geologic Characteristics of the Chang'E-3 Exploration Region. *Science China Physics, Mechanics and Astronomy*, 57(3): 569–576. doi:10.1007/s11433-014-5399-z
- Zhao, N., Zhu, P. M., Yang, K. S., et al., 2014. The Preliminary Processing and Analysis of LPR Channel-2B Data from Chang'e-3. *Science China Physics, Mechanics & Astronomy*, 57(12): 2346–2353. doi:10.1007/s11433-014-5590-2